

The challenging task of determining star formation rates: the case of a massive stellar burst in the brightest cluster galaxy of Phoenix galaxy cluster

Rupal Mittal^{1,2*}, M. McDonald³, John T. Whelan⁴, Gustavo Bruzual⁵

¹ *Max-Planck-Institut für Gravitationsphysik (Albert-Einstein-Institut), D-30167 Hannover, Germany*

² *Rochester Institute of Technology, 54 Lomb Memorial Drive Rochester, NY, USA 14623*

³ *MIT Kavli Institute for Astrophysics and Space Research*

⁴ *School of Mathematical Sciences and Center for Computational Relativity and Gravitation, Rochester Institute of Technology, Rochester, NY 14623, USA*

⁵ *Instituto de Radioastronomía y Astrofísica, UNAM, Campus Morelia, C.P. 58089, Morelia, México*

Received/Accepted

ABSTRACT

Star formation in galaxies at the center of cooling-flow galaxy clusters is an important phenomenon in the context of formation and evolution of massive galaxies in the Universe. Yet, star formation rates (SFRs) in such systems continue to be elusive. We use our Bayesian-motivated spectral energy distribution (SED)-fitting code, `BAYESCOOL`, to estimate the plausible SFR values in the brightest cluster galaxy of a massive, X-ray luminous galaxy cluster, Phoenix. Previous studies of Phoenix have resulted in the highest measurement of SFR for any galaxy, with the estimates reaching up to $1000 M_{\odot} \text{ yr}^{-1}$. However, a very small number of models have been considered in those studies. `BAYESCOOL` allows us to probe a large parameter space. We consider two models for star formation history, instantaneous bursts and continuous star formation, a wide range of ages for the old and the young stellar population, along with other discrete parameters, such as the initial mass function, metallicities, internal extinction and extinction law. We find that in the absence of any prior except that the maximum cooling rate $< 3000 M_{\odot} \text{ yr}^{-1}$, the SFR lies in the range $(2230 - 2890) M_{\odot} \text{ yr}^{-1}$. If we impose an observational prior on the internal extinction, $E(B-V) \leq 0.6$, the best-fit SFR lies in $(454 - 494) M_{\odot} \text{ yr}^{-1}$, and we consider this as the most probable range of SFR values for Phoenix. The SFR dependence on the extinction is a reflection of the standard age-extinction degeneracy, which can be overcome by using a prior on one of the two quantities in question.

Keywords: galaxies: clusters: intracluster medium ; galaxies: clusters: individual: SPT-CLJ2344-4243 ; galaxies: formation ; galaxies: star formation ; ISM:) dust, extinction

1 INTRODUCTION

The last decade has witnessed tremendous progress in the field of cooling flows in galaxy clusters, both observationally and theoretically. Observationally, there seems to be a sharp threshold in cooling time (e.g. Hudson et al. 2010) or equivalently central entropy (e.g. Cavagnolo et al. 2009) below which there is clear evidence of cooling (1) in the form of cold gas, such as $H\alpha$ filaments (Heckman et al. 1989; Crawford et al. 1999; Conselice et al. 2001; McDonald et al. 2012), CO emission (Edge 2001; Edge et al. 2002; Salomé et al. 2008), FIR emission (Edge et al. 2010a,b; Mittal et al. 2011, 2012; Rawle et al. 2012), (2) in the form of presence of an AGN (e.g. Mittal et al. 2009) and (3) in the form of star formation (e.g. Hicks & Mushotzky 2005; O’Dea et al. 2008; McDonald et al. 2011; Mittal et al. 2015; Tremblay et al. 2015). These observations can now be understood in terms of a particular quantity first introduced by Sharma et al. (2012). Their numerical simulations show that formation of multi-phase filaments depend upon the ratio, $r = t_{\text{ff}}/t_{\text{H}}$, of the growth time of the thermal instability to the

free-fall time. When this ratio falls below a certain threshold, the local thermal instabilities cause the temperature and density fluctuations to become non-linear and the gas quickly cools. The cold gas decouples from the hot intracluster medium (ICM) and produces spatially-extended $H\alpha$ filaments. These cold clumps can either rain down on the supermassive black hole or contribute to star formation (e.g. Gaspari et al. 2012; Li et al. 2015). It is this cold accretion that triggers AGN activity that heats up the cluster atmospheres. The AGN heating eventually drives this ratio to go above 10, which halts any further precipitation and subsequently the AGN activity. This marks the beginning of another cycle of ICM cooling, followed by star formation and AGN-heating.

Despite the aforementioned observational and theoretical progress, star formation rates (SFRs) in the brightest cluster galaxy of such cool-core systems are still very poorly constrained with an unacceptably wide discrepancy between different estimates, and are an impediment preventing development of a coherent narrative. The chief limitation of the existing methods of determining star formation rates (based on the measurement of emission lines, such as $H\alpha$,

arXiv:1611.02562v2 [astro-ph.GA] 16 Jan 2017

or FUV–NUV colour or infrared luminosity) is that there exist *degeneracies* in that different combinations of the model parameters can result in the same observed spectral energy distribution (SED). This is the underlying reason for the widely discrepant estimates of star formation rates existing in the literature. As an example, O’Dea et al. (2010) used FUV emission to estimate an SFR of $12 M_{\odot} \text{ yr}^{-1}$ in the BCG of A 1835 on the one extreme (the study does not mention any errorbars) and Hicks & Mushotzky (2005) used UV-excess to estimate an SFR of $(226 \pm 9) M_{\odot} \text{ yr}^{-1}$ on the other. Such a dispersion in results is in most part due to the different assumptions made about the star formation history, particularly the age and mass of the young stellar population.

A Bayesian approach is optimal for such a situation since, given a prior probability of the parameters (uniform in the simplest case), it considers all possible combinations of parameters and provides statistically-derived probability distributions for each parameter. In Mittal et al. (2015), we studied the star formation histories of the brightest cluster galaxies in 10 cool-core galaxy clusters (hereon we refer to a brightest cluster galaxy in a cool-core galaxy cluster as “cool-core BCGs”). We used a Bayesian-motivated SED-fitting model, *BAYESCOOL*, wherein we let the physical parameters vary over realistic ranges, and implement marginalization technique to get posterior probability distributions for the model parameters and quantities derived from them (such as SFRs). As shown by Conroy et al. (2010); Pforr et al. (2012); Walcher et al. (2011), integrated light from galaxies at points of the SED sampled well enough can be used to constrain the basic parameters, provided that marginalization techniques are used to incorporate the uncertainties in the model.

Constraining the star formation history is imperative for cooling-flow clusters to be better able to link the cooling of the ICM, star formation and active galactic nuclei (AGN)-regulated feedback. In Mittal et al. (2015), we find that 9 out of 10 BCGs have been experiencing starbursts since 6 Gyr ago. While 4 out of 9 BCGs seem to require continuous star formation, 5 out of 9 seem to require periodic star formation on intervals ranging from 20 Myr to 200 Myr. This time scale is similar to the cooling-time of the intracluster gas in the very central (< 5 kpc) regions of BCGs. These results are just the tip of the ice-berg within the paradigm, where multiple epochs of cooling, star formation and AGN heating are expected to occur.

Similarly, detailed information on the star formation history of a galaxy also allows us to establish whether or not there is a link between star formation and AGN heating. In Mittal et al. (2015), while we find no relation between the BCG radio luminosity and SFRs (in accordance with the results of Li et al. 2015), 4 out of 5 BCGs requiring multiple outbursts have the highest radio luminosities. This agrees with the theoretical model of Sharma et al. (2012), where once the gas starts cooling, some of it is clumped into molecular clouds leading to star formation and some of it serves as fuel for the AGN.

In this paper, we apply *BAYESCOOL* to estimate the star formation rate in the brightest galaxy of the Phoenix cluster of galaxies, SPT-CLJ2344-4243, at a redshift of $z = 0.596$ (we refer to the BCG as simply “Phoenix” hereafter). The Phoenix galaxy cluster, although a relatively recent discovery by the South Pole Telescope using the Sunyaev-Zeldovich (SZ) effect (Williamson et al. 2011; McDonald et al. 2012), has an acclaimed status owing to its high X-ray luminosity, $L_{(2-10)\text{keV}} = 8.2 \times 10^{45} \text{ erg s}^{-1}$, and the largest predicted cooling-flow rate (the X-ray mass deposition rate) known-to-date of about $(3300 \pm 200) M_{\odot} \text{ yr}^{-1}$ in the inner 100 kpc (McDonald et al. 2013). It is further host to a massive reservoir of molecular

gas ($M_{H_2} \sim 2 \times 10^{10} M_{\odot}$ McDonald et al. 2014), and a dusty type-II quasar (e.g. Ueda et al. 2013).

The aspect that makes this cluster of further particular interest is the ongoing star formation rate in Phoenix inferred using different techniques and based on different assumptions, with estimates ranging from about $400 M_{\odot} \text{ yr}^{-1}$ to about $1500 M_{\odot} \text{ yr}^{-1}$ (McDonald et al. 2012). The study by McDonald et al. (2013) used five HST/WFC3 broad-band filters and presented a UV-derived revised estimate of $(798 \pm 42) M_{\odot} \text{ yr}^{-1}$, assuming a mean internal extinction of $E(B - V) = 0.34$. However, more recent results of McDonald et al. (2015) from an analysis combining the previous HST/WFC3 broad-band filters along with HST/COS FUV and Gemini-S GMOS optical spectroscopy suggests an SFR of about $(300 - 500) M_{\odot} \text{ yr}^{-1}$. This range reflects the uncertainty in internal extinction and the dependence of the result on the *only* two star formation history scenarios considered that give the lowest least-square-fit residuals – (1) continuous star formation since 15 Myr ago, (2) an instantaneous burst that occurred 4.5 Myr ago.

The above summary of the efforts made to estimate the SFR in Phoenix far under-states the detailed analysis and assumptions made at each step. Estimating star formation rates in galaxies is a task far from simple. There exist numerous theoretical and empirical relations that connect observables to a star formation rate. Most of these relations, if not all, are based on stellar population synthesis (SPS), where a star formation history (SFH) along with an initial-mass-function (IMF), a metallicity, an extinction law and internal reddening is assumed, reflecting a large parameter space. It is common to use supplementary diagnostics to narrow down the range of parameters but such diagnostic tools rely on yet another set of assumptions. For example, the use of Balmer emission lines, assuming case-A (assuming optically-thin nebula) or -B (assuming optically-thick nebula) recombination, is standard to constrain the internal reddening. In *BAYESCOOL*, we simply relax the various assumptions and use the underlying SPS spectra directly to determine what the data are telling us. Bayesian marginalization circumvents the issue of a large parameter space by considering as many models as computational resources allow us in obtaining meaningful ranges of parameter values.

Despite the large uncertainty in the current estimates of the SFR, it is clear that the BCG of Phoenix harbours a massive starburst ($> 100 M_{\odot} \text{ yr}^{-1}$). There are very few cooling-flow clusters with such high SFRs. In general, the SFRs in known cool-core clusters are lower than the classical cooling-flow rates by factors of 5 to 100 (e.g. Mittal et al. 2015; O’Dea et al. 2008). However, it may very well be that this observation is due to the lack of a consideration of models that lead to higher SFRs, and the likelihood of such models. McDonald et al. (2015) postulate that the vast supply of cold gas as seen in Phoenix is a feature of a classical cooling-flow model. The AGN in Phoenix is unique in that it is indicative of both a strong radiative (quasar) mode and a strong mechanical (radio) mode activity. A large star formation rate then implies that the AGN-feedback has not yet coupled with the cooling of the intracluster medium. In order to be able to make any robust interpretations, it is crucial that we first make a determination of a *reliable* range of SFRs considering all possible values of the model parameters, so that we may better address the order of magnitude discrepancy in mass deposition rates in cooling-flow models, and the exact processes regulating star formation in some of the most massive galaxies in the Universe.

We assume throughout this paper the Λ CDM concordance Universe, with $H_0 = 71 h_{71} \text{ km s}^{-1} \text{ Mpc}^{-1}$, $\Omega_m = 0.27$ and $\Omega_{\Lambda} = 0.73$ (Larson et al. 2011; Jarosik et al. 2011). The Galactic

extinction towards the line-of-sight of Phoenix is $E(B-V) = 0.016$, which is small as compared to the internal extinction (both previously known and that derived in this paper), and hence we ignore it. Moreover, since the extinction is additive in nature, the true internal extinction can be derived by subtracting the Galactic extinction from the total extinction.

2 DATA ACQUISITION AND ANALYSIS

The data used to create the spectral energy distribution for Phoenix shown in Figure 3 are described below.

2.1 HST WFC3-UVIS: Broad-Band Optical Photometry

We include in this paper optical broad-band imaging from the *Hubble Space Telescope* Wide Field Camera 3 (HST WFC3-UVIS). Data in five bands (F225W, F336W, F475W, F625W, F814W) were acquired using Director’s Discretionary Time (PID 13102, PI: McDonald) in the 2012. These data were reduced using the standard STScI pipeline, with cosmic rays removed in each individual frame using the LA Cosmic software (van Dokkum 2001). A more detailed description of these data are presented in McDonald et al. (2013).

For each filter, we extract the total flux within an aperture roughly $3''$ (20 kpc) in radius, which is large enough to enclose the majority of the flux from all bands (see Figure 3 from McDonald et al. 2013).

2.2 Gemini GMOS: Optical Spectroscopy

Optical spectroscopy used in this paper were obtained using the GMOS-S IFU on Gemini South. These data span (5360–9600) Å in the observed frame, corresponding to (3356–6011) Å in the rest frame. The full field of view for these data is $9'' \times 5''$. For a full description of the data acquisition and analysis, the reader is directed to McDonald et al. (2014). The optical spectrum of the central galaxy was extracted in the same aperture as described above for the broad-band data.

2.3 HST COS: Ultraviolet Spectroscopy

Far-UV spectroscopy for the central galaxy in the Phoenix cluster was obtained using the Cosmic Origins Spectrograph on the *Hubble Space Telescope* (HST-COS; ID 13456, PI: McDonald). The data used in this paper consist of two aperture spectra, each having a $2.5''$ diameter. The combined footprint for these apertures is roughly $4'' \times 2.5''$. The relative positioning of the two pointings yields roughly 80%–100% throughput over the full region for which there is bright UV emission (i.e., the galaxy center). The full details of these observations and their reduction are presented in McDonald et al. (2015).

We matched the aperture of the three instruments by extracting aperture spectra from the GMOS and HST broad-band filters and matching the COS throughput as a function of radius within that aperture. While best efforts were made to ensure that the three datasets reflected the same region in the sky, there could still be some remaining offsets between the instruments. However, we suspect those offsets to be within the data uncertainties.

3 AGN AND DUST CONTAMINATION

X-ray *Chandra* data shows that the central 10 kpc is dominated by a point-source emission in the (2-8) keV band, which is very likely an AGN. Diagnostic line ratios suggest a Seyfert-like component in the nucleus, corresponding to the AGN, and LINER-like component in the extended regions, corresponding to the cool-core filaments, likely excited by young stars and shocks (McDonald et al. 2012). The AGN is also observed to be radio loud ($\nu L_\nu = 10^{42}$ erg s $^{-1}$) (Mauch et al. 2003), albeit with radio luminosity far lower than the cooling luminosity. The central source, based on the high far-infrared luminosity, together with the hard X-ray and radio luminosity of the AGN, is considered to be dusty, highly-obscured. McDonald et al. (2013) argue based on further HST UV data, along with the lack of UV emission along the minor axis of the central galaxy, that the AGN contribution to the UV luminosity is small ($< 10\%$). In the analysis to follow, hence, we work under the assumption that the AGN contribution to the spectral energy distribution of the galaxy may be ignored. The reader is referred to McDonald et al. (2012, 2013) for detailed work on the AGN in Phoenix and its characteristics, providing justification for this assumption.

Most observations of Phoenix point to a very dusty system with a possibly high internal reddening to the extent of $E(B-V)$ being close to 0.6. However, the aim of applying BAYESCOOL is to explore the stellar population parameters. While we may easily incorporate the plethora of available infrared data, and thereby increase the number of constraints, experience tells us that fitting accurate dust parameters (the number of thermal dust components along with their masses, temperatures and the dust absorption coefficient) is another task in itself, which not only entails making assumptions on the dust model parameters, but also about the background stellar radiation. The latter defeats the purpose of trying to determine the various stellar populations and the physical parameters thereof. Furthermore, since our analysis is based on using a minimum number of assumptions, one of the requirements becomes to avoid fitting any thermal dust components. Hence, we restrict our analysis to using data up to an observed-frame wavelength of around $1 \mu\text{m}$.

4 BAYESIAN METHOD

Here we describe the details of our code, BAYESCOOL. The basic method was described in detail in Mittal et al. (2015); we recap the key features here. Note that BAYESCOOL is very similar to iSEDfit (Moustakas et al. 2013) but the two works are independent and differ in their motivation (BAYESCOOL derives its motivation from the existing dispersion in the SFR estimates, specifically, in cool-core BCGs). Using the SEDs generated with integrated flux-densities (using any available data, broad-band and/or spectroscopic), we fit the data with a model comprising an old stellar population (OSP) and a young stellar population (YSP), each of which has at least two parameters – the age and the total mass. In Mittal et al. (2015), we hypothesized that the normalization of the SED corresponding to a synthetically generated stellar population scales linearly with the total mass in the stars. Assuming that the mass and the age are the only two parameters, the flux density at any given frequency, i , may be written in the form, $F_i(M, T) = M \times S_i(T)$, where M is the total mass and T is the age of the population. $S_i(T)$ is the flux density per unit mass, which depends on the age. Now, we extend this ansatz to include other model parameters.

We have a series of flux measurements $\{F_i\}$ with associated

weights $\{w_i\}$, where $1/\sqrt{w_i}$ is the 1σ uncertainty associated with F_i . Given a family of models H parametrized by YSP mass M_y , OSP mass M_o , and some other (discretely-sampled) parameters θ , if the errors on the F_i are assumed to be independent and Gaussian, Bayes's theorem allows us to construct a posterior probability distribution

$$P(M_o, M_y, \theta | \{F_i\}, H) \propto P(M_o, M_y, \theta | H) \exp\left(-\frac{\chi^2(M_o, M_y, \theta)}{2}\right) \quad (1)$$

$$\text{where } \chi^2(M_o, M_y, \theta) = \sum_i w_i [F_i - M_o S_i^{(o)}(\theta) - M_y S_i^{(y)}(\theta)]^2, \quad (2)$$

$S_i^{(o)}$ and $S_i^{(y)}$ are the flux per unit mass contributions from the OSP and YSP, respectively. The total observed flux at a given frequency, i , is assumed to be equal to

$$\begin{aligned} F_i(\theta) &= F_i^{(o)}(\theta) + F_i^{(y)}(\theta) = M_o S_i^{(o)}(\theta) + M_y S_i^{(y)}(\theta) \\ &= M_o S_i^{(o)}(\theta) + M_y \sum_{n=1}^{N_{\text{bursts}}} S_{i,n}^{(y)}(\theta) \end{aligned} \quad (3)$$

where $F_i^{(o)}$ and $F_i^{(y)}$ are the flux contributions from the OSP and YSP, respectively, and N_{bursts} are the number of bursts of star forming episodes. θ includes the age of the OSP, τ_o , and the age of the YSP, τ_y . To simplify both the approach and the calculations, we assume uniform priors, specifically uniform density in M_y and M_o , with the only restriction being $0 < M_y < M_o$, and that each of the discrete values of extinction, metallicity and τ_o , and the different possibilities for IMF and extinction law, are independently equally likely. Since we consider multiple-starburst models with N_{bursts} bursts evenly spaced in age from τ_y to $N_{\text{bursts}}\tau_y$, we consider each of the discrete ($N_{\text{bursts}}, \tau_y$) combinations sampled to have equal prior probability.

From the posterior probability, we can calculate useful probability distributions for various variables, marginalized over the others, such as the posterior probability density for the masses

$$P(M_y | \{F_i\}, H) = \sum_{\theta} \int_{M_y}^{\infty} dM_o P(M_o, M_y, \theta | \{F_i\}, H) \quad (4)$$

$$P(M_o | \{F_i\}, H) = \sum_{\theta} \int_0^{M_o} dM_y P(M_o, M_y, \theta | \{F_i\}, H) \quad (5)$$

or the posterior probability distribution $P(x | \{F_i\}, H)$ for a discretely-sampled or categorical variable x which is among the parameters θ , whose value at some $x = x_0$ is

$$P(x_0 | \{F_i\}, H) = \sum_{\theta: x=x_0} \int_0^{\infty} dM_o \int_0^{M_o} dM_y P(M_o, M_y, \theta | \{F_i\}, H) \quad (6)$$

By similar means, posterior probability densities can be constructed for derived quantities such as the mass ratio M_y/M_o and star formation rate¹ $M_y/(N_{\text{bursts}}\tau_y)$.

5 STELLAR POPULATION SYNTHESIS

5.1 Model Parameters

In order to create synthetic stellar spectra, we used the publicly available library of evolutionary stellar population synthesis models, GALAXEV, released by G. Bruzual and S. Charlot (Bruzual &

Charlot 2003). To use the Bruzual & Charlot (2003) models in the present version of BAYESCOOL, we modified the tools provided in the GALAXEV package to sample the evolving stellar population every 1 Myr. This allows for a finer sampling of the successive star bursts in the SSP models than if we use the standard time scale. The modified software is available upon request from Gustavo Bruzual.

The model parameters and the number of types/values they can assume are (the range and step-size where relevant are given within square-brackets):

- Initial Mass Function, IMF: 3 [Chabrier, Salpeter, Kroupa]
- Extinction laws: 2 [Galactic, extragalactic]
- Metallicities, Z: 3 [0.4 solar, solar and 2.5 solar]
- Internal Reddening, $E(B - V)$: 15 [0 to 1.4 in steps of 0.1]
- YSP age, τ_y : 6000 [1 Myr to 6 Gyr in steps of 1 Myr]
- OSP age, τ_o : 7 [3 Gyr to 6 Gyr in steps of 0.5 Gyr]
- Star Formation History, SFH: 2 [continuous star formation, instantaneous burst]

We terminate both the OSP and YSP age at 6 Gyr because of the maximum allowed age for Phoenix equal to the age of the Universe at the formation redshift of the OSP, assumed to be $z_f = 3$, minus its light-travel time. The detailed description of the model parameters can be found in (Mittal et al. 2015). The only differences between the present study and that described in Mittal et al. (2015) are that in the current study (1) the spacing between bursts is smaller (10 Myr vs 1 Myr) and (2) we consider both continuous star formation (CSF) as well as instantaneous bursts (or simple stellar populations, SSP) whereas in Mittal et al. (2015) we considered only the latter. While both CSF and SSP star formation history models follow equation 4, only the SSP models have N_{bursts} other than 1.

Our model allows the possibility of the YSP components to begin as early as $z \sim 3$ since several studies (e.g. Eisenhardt et al. 2008; Mei et al. 2009; Mancone et al. 2010; Brodwin et al. 2013; Alberts et al. 2014) indicate a model in which the stellar component in galaxies in cluster centers may have formed as a result of multiple bursts of vigorous star formation at redshifts as recent as $z \sim 1.5$. Furthermore, there is no theoretical argument why stellar bursts could not have occurred right after the massive old stellar population was assembled through mergers. For Phoenix, however, there is no need as such to impose this requirement since the spectral energy distribution seems to strongly indicate a star formation history based on a single, rather young, stellar population. (Section 5.3).

The expected cooling-flow rate, which essentially includes the mass of the total gas that is available to be churned into stars, and the shortest time scale over which this can happen (since the gas must cool down to very low temperatures, < 10 K to form stars), sets the upper limit to the star formation rate. The expected cooling-flow value on the scale of the galaxy (20 kpc) is about (2000 to 3000) $M_{\odot} \text{ yr}^{-1}$, and we use this as a prior for our simulations.

5.2 Data Uncertainties

As mentioned in 2, we use both imaging and spectral data for the SED. An important consideration to bear in mind are the weights assigned to the data from each category. The overall errorbars (random as well as absolute) associated with both the imaging and spectral data are typically (10 – 20)%. However, the imaging data at 2371 Å, 3353 Å and 4770 Å are sparsely populated in wavelength. The spectral resolution of HST/COS FUV data is about 1 Å/pix and

¹ Since M_y is the total mass in the YSP, the mass in each starburst is M_y/N_{bursts} .

that of Gemini-S GMOS is about $4 \text{ \AA}/\text{pix}$. In comparison, the root-mean-square bandwidths of the HST/WFC3 filters F225W, F336W and F475W are 177 \AA , 158 \AA and 421 \AA , respectively. So that the spectral data (densely populated) and these three broad-band datapoints are considered at the same footing during the fitting, we increased the weights associated with the latter by a factor of about 50, corresponding to a decrease in their errorbars by a factor of about 7 (since $w_i = 1/\sigma^2$), i.e. reducing the uncertainty of the (2000-5000) \AA broad-band data from 15% to 2.5%. However, the final results do not seem to be sensitive to the errorbars associated with the (2000-5000) \AA broad-band data in that the most probably values of the model parameters do not change significantly as the errorbars are reduced from 15% to 2.5%.

5.3 Results

We show in Figure 1 the posterior probability distributions for all the model parameters, where we allowed them to vary over the respective ranges defined in Section 5.1, with the only restriction being that the posterior probability distribution for the SFR does not exceed $3000 M_{\odot} \text{ yr}^{-1}$.

While the data clearly rule out the Salpeter-type IMF, they are not able to distinguish between the Kroupa- and Chabrier-type (top left panel). In fact, both the IMFs have about 50% likelihood of fitting the data. This is not surprising given the similarities between the Chabrier and the Kroupa IMFs at the low mass end. The main difference between Salpeter-type IMF and the other two is that the former predicts a higher number of low-mass stars.

5.3.1 Internal Extinction

The internal extinction (shown in the top middle panel of Figure 1), on the other hand, has a single peak at $E(B - V) = 0.9$. This value is larger than the previous measurements made using the Balmer line ratios implying $E(B - V)$ in the range between 0.3 and 0.4 (McDonald et al. 2012). In a later study, McDonald et al. (2013) published a 2D reddening map, where the authors deduced reddening values using HST F336W and F475W images, assuming a flat SED in the absence of reddening (Kennicutt 1998). Their results based on this assumption show that $E(B - V)$ ranges from small values (< 0.1) away from the outer star-forming regions to 0.6 at the very center. Our results show that the most plausible value of the average extinction in Phoenix is higher than any of the previous measurements.

5.3.2 Star Formation History

The posterior probability distribution for the star formation history (top right panel) reveals that simple stellar populations (a series of instantaneous bursts) fit the data with a somewhat higher likelihood than continuous star formation (the latter has about 35% posterior probability distribution). The N_{bursts} versus τ_y plot further points to a scenario that contains a series of four bursts a Myr apart. Note that a model comprising four bursts a Myr apart is considered a single model and not four separate models.

In view of the high extinction value and a very young stellar population, it is not surprising that the star formation rate lies in the range (2000 to 3000) $M_{\odot} \text{ yr}^{-1}$ (center right panel). This is, in fact, consistent with a star formation rate of $\sim 800 M_{\odot} \text{ yr}^{-1}$ as estimated by McDonald et al. (2013) assuming an extinction of 0.6. If the extinction is considered to be 0.9 instead, the extinction-corrected

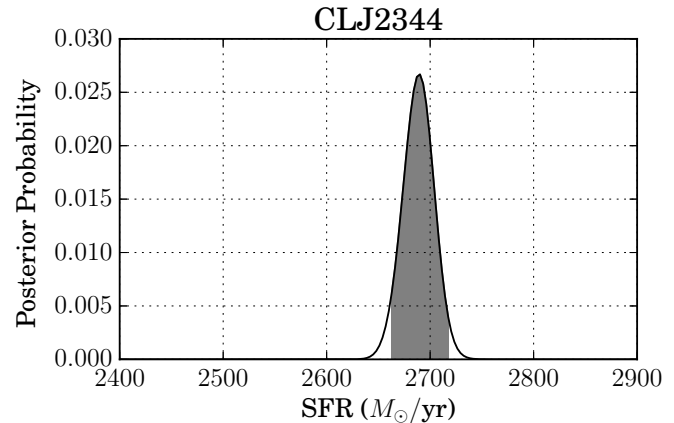


Figure 2. Posterior probability distribution for the star formation rate with the initial mass function (IMF) fixed to Chabrier and the star formation rate fixed to simple stellar population (SSP). There is a single peak at $SFR \sim 2690 M_{\odot} \text{ yr}^{-1}$.

flux increases by a factor of three to four at an assumed observed-frame wavelength of 4000 \AA . This amounts to an equivalent increase in star formation rate using the Kennicutt (1998) UV-to-SFR conversion. This back-of-envelope calculation implies a large range of possible SFRs in the absence of an accurate knowledge of the internal extinction.

According to the posterior probability distribution of the age of the old stellar population (the lower most panel of Figure 1), the likelihood increases from 3.5 Gyr to 5.5 Gyr and then sharply (with $\sim 50\%$ posterior probability) to 6 Gyr, implying that the oldest generation stars came into existence at $z \sim 3$ (or at an even later redshift, a scenario not included in our simulations).

5.3.3 Star Formation Rate

The posterior probability distribution of the SFR (center middle panel) is quadrimodal and imply a star formation rate in the range $2230 - 2890 M_{\odot} \text{ yr}^{-1}$. The four different peaks point to the degeneracies in the initial mass function (Kroupa vs Chabrier) and also the star formation history in commensurate measure. The two lower peaks correspond to the CSF models and the two higher peaks correspond to the SSP models. For example, if the IMF was fixed to Chabrier and the SFH to SSP, the resulting posterior probability distribution for the SFR will appear as shown in figure 2, with a single clear peak at $SFR \sim 2690 M_{\odot} \text{ yr}^{-1}$. Similarly, the posterior probability distribution of the SFR for the case where the extinction, $E(B - V)$, is limited to 0.6 shows a bimodal distribution due to the degeneracy in the IMF (the data support only CSF models for the prior, $E(B - V) < 0.6$, hence there are only two peaks).

We tabulate the most likely values of the model parameters in Table 1 considering three scenarios. The first scenario corresponds to the best-fit values when all the parameters are allowed to vary under the restriction that the $SFR < 3000 M_{\odot} \text{ yr}^{-1}$. The second scenario corresponds to the best-fit values with the added constraints that the IMF is Chabrier and the SFH is SSP-type. The third scenario corresponds to the best-fit values when we use the prior, $E(B - V) < 0.6$, which is the upper limit inferred by McDonald et al. (2014) using the Balmer emission lines. We quote the mean and the 68% plausible interval, the narrowest interval which contains 68% of the area under the posterior probability density

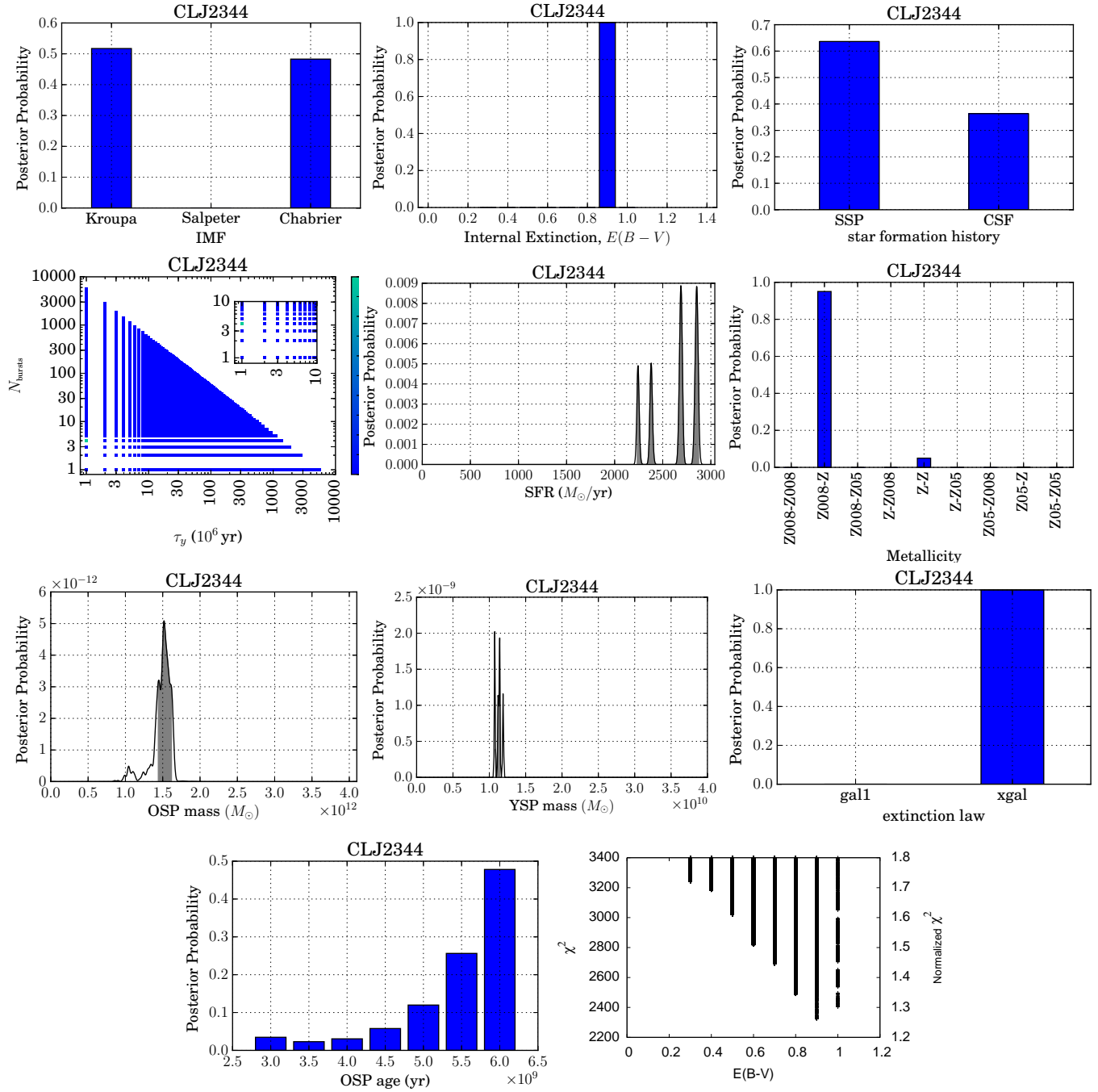


Figure 1. Posterior probability distributions for the various model parameters using the prior $SFR < 3000 M_{\odot} \text{ yr}^{-1}$ – *first row (left):* initial mass function, *first row (middle):* internal extinction, *first row (right):* star formation history, *second row (left):* N_{bursts} vs spacing between the bursts (note that in this case significant posterior support exists only for the model with $N_{\text{bursts}} = 4$ and $\tau_y = 1$ Myr), *second row (middle):* star formation rate, *second row (right):* metallicity, *third row (left):* OSP mass, *third row (middle):* YSP mass, *third row (right):* extinction law, *bottom row (left):* OSP age and *bottom row (right):* χ^2 as a function of internal extinction.

function, for all parameters except the SFR for which we consider the 95% plausible interval.

The star formation rate for the case where the internal extinction is restricted to be $E(B - V) \leq 0.6$, as the observations suggest, yields a star formation rate in the range $(454 - 494) M_{\odot} \text{ yr}^{-1}$. We regard the best-fitting model obtained with $E(B - V) \leq 0.6$ as the most reliable model for Phoenix, and hence the SFRs in the above range as the most probable values.

Even though the SFR value of $490 M_{\odot} \text{ yr}^{-1}$ inferred by McDonald et al. (2015) before making the HST-COS aperture correction lies in the above range, the results of that work were incorrect by a factor of $(1 + z)$, where $z = 0.596$. After correcting the fluxes by this factor, the star formation rate from the work of McDonald et al. (2015) is about $780 M_{\odot} \text{ yr}^{-1}$ (assuming other model parameters do not change). This is higher than what we obtain due to the fact that while the best-fitting YSP model in McDonald et al.

Table 1. The most likely physical parameters of the stellar populations in the BCG of the Phoenix galaxy cluster, assuming the SFR $< 3000 M_{\odot} \text{ yr}^{-1}$. “PI” refers to the narrowest 68% plausible interval for all parameters except the star formation rate for which it refers to the narrowest 98% plausible interval. $\tau_{y,\text{old}}$ refers to the age of the oldest YSP. It is relevant only in the case $N_{\text{bursts}} > 1$. For SFH=SSP only, $\tau_{y,\text{old}} = N_{\text{bursts}} \times \tau_y$.

Parameter	All parameters free		Priors: SFH=SSP, IMF=Chab.		Priors: $E(B-V) \leq 0.6$	
	Mean	PI	Mean	PI	Mean	PI
M_y ($10^{10} M_{\odot}$)	1.11	1.07 – 1.14	1.08	1.07 – 1.08	2.10	1.98 – 2.24
$\tau_{y,\text{old}}$ (Myr)	4.4	3.5 – 4.5	4	–	44.4	41.5–46.5
M_o ($10^{11} M_{\odot}$)	15.3	14.4 – 16.2	15.0	14.3 – 15.7	12.24	11.51 – 12.96
τ_o (Gyr)	6	–	6	–	6	–
SFR	quadrимodal	2230 – 2870	2690	2660 – 2720	bimodal	454 – 494
SFH	SSP	$N_{\text{bursts}} = 4, \tau_y = 1 \text{ Myr}$	–	$N_{\text{bursts}} = 4, \tau_y = 1 \text{ Myr}$	CSF	–
$E(B-V)$	0.9	–	0.9	–	0.6	–
$Z_{\text{y sp}}$	Z_{\odot}	–	Z_{\odot}	–	$2.5Z_{\odot}$	–
Z_{osp}	$0.4Z_{\odot}$	–	$0.4Z_{\odot}$	–	$0.4Z_{\odot}$	–
IMF	Kroupa/Chab.	–	–	–	Kroupa/Chab.	–
Extinction Law	XGAL	–	XGAL	–	XGAL	–

The model parameters are the mass of the young and old stellar population, M_y and M_o , the age of the young and old stellar population, τ_y and τ_o , the star formation rate, SFR, the internal reddening, $E(B-V)$, the metallicity of the young and old stellar population, $Z_{\text{y sp}}$ and Z_{osp} , the initial mass function, IMF, and the extinction law.

(2015) corresponds to an instantaneous burst that occurred 4.5 Myr ago, the best-fitting YSP model from our work (using the prior, $E(B-V) < 0.6$) corresponds to continuous star formation occurring over the past ~ 44 Myr ago. However, McDonald et al. (2015) considered only a few models (< 100) compared to the ~ 200 million models considered in this study. A CSF model with $\tau_y = 45$ Myr was not tried.

5.3.4 An example plot

Shown in Figure 3 in an *example* best-fit plot created by fixing the model parameters to their most likelihood values using the prior $E(B-V) \leq 0.6$. Note that there are many more models with slightly different combinations of model parameters that are capable of reproducing the observed SED with the same degree of goodness-of-fit. The errorbars on the most likelihood parameters encapsulate all those models and this highlights the strength in Bayesian marginalization. The red curve depicts the flux contribution by the OSP and the blue curve depicts the net-flux contribution by the YSP. The bottom panel of Figure 3 shows the significance of the OSP at observed-frame wavelengths beyond 5000 Å and, therefore, the importance of fitting both the old and young stellar component simultaneously.

The best-fit model at the high-frequency end of the HST-COS data (1400 Å to 1500 Å) are not as well explained by the model as the rest of the data. This can be due to the fact that our analysis includes only two families of models (continuous star formation and a superposition of periodically-based bursts). However, we do not expect these data to affect significantly our estimates of the parameters in the current models since this is a small fraction of data points (4%). In future analyses, we aim to expand our code to include multiple stellar populations (non-periodic) and other families of SFH, such as exponential-declining star formation, stellar bursts of certain length, delayed star formation, all of which are available within GALAXEV. Similarly, we aim to work with a finer grid of discrete variables (metallicity and also evolutionary tracks), which along with a new set of stellar spectra designed to model nebular emission in star-forming galaxies, particularly over UV and optical range, have recently become available within GALAXEV. As an

example, a crude exercise shows that the break observed around 1450 Å can be reproduced by adding together SEDs corresponding to 6 Myr and 120 Myr stellar populations with a metallicity of $Z = 0.017$ and Chabrier IMF. We also aim to modify our code as to allow the parameters of the extinction law vary (see Section 6.4). This will affect the highest frequency data the most since extinction scales with frequency. Finally, we plan to generalize the current model of independent uncertainties associated with the data points $\{F_i\}$ with a more general framework including correlations among nearby frequencies and/or within the spectroscopic sample from each instrument. While we have made an attempt to match apertures between different data sources, there may still be aperture effects that could lead to slight normalization offsets and the above generalization will account for this.

6 DISCUSSION

It is worth considering another scenario where we do not impose the SFR $< 3000 M_{\odot} \text{ yr}^{-1}$ restriction. By considering all models with no restriction on SFR yields an even higher best-fit extinction, $E(B-V) = 1.1$, and a continuous star formation that commenced 3 Myr ago with the cumulative mass three times more than that listed in Table 1. These properties result in an enormous SFR of about (12000–13000) $M_{\odot} \text{ yr}^{-1}$. A recent study conducted by Prasad et al. (2015) probed the evolution of cool cluster cores in the presence of bipolar AGN feedback based on hydrodynamic simulations. Their results show that even though the average SFR is suppressed by AGN feedback over gigayear timescales, the instantaneous cold gas mass-inflow rate may be similar or even higher than the cooling flow value, depending upon the region considered where the gas condenses profusely (on the scale of a few kpc) and the feedback efficiency parameter. This is a direct consequence of multi-phase cooling. Once the multi-phase cooling initiates, the condensation of gas can proceed at almost the free-fall time. Under these conditions, the instantaneous SFR timescale may be as short as the dynamical time. So while a star formation rate in Phoenix much greater than the cooling-flow rate is physically possible, it is unlikely that we have caught the system in a state with a likelihood of 5%-10% Prasad et al. (2015). Moreover, the observations of Mc-

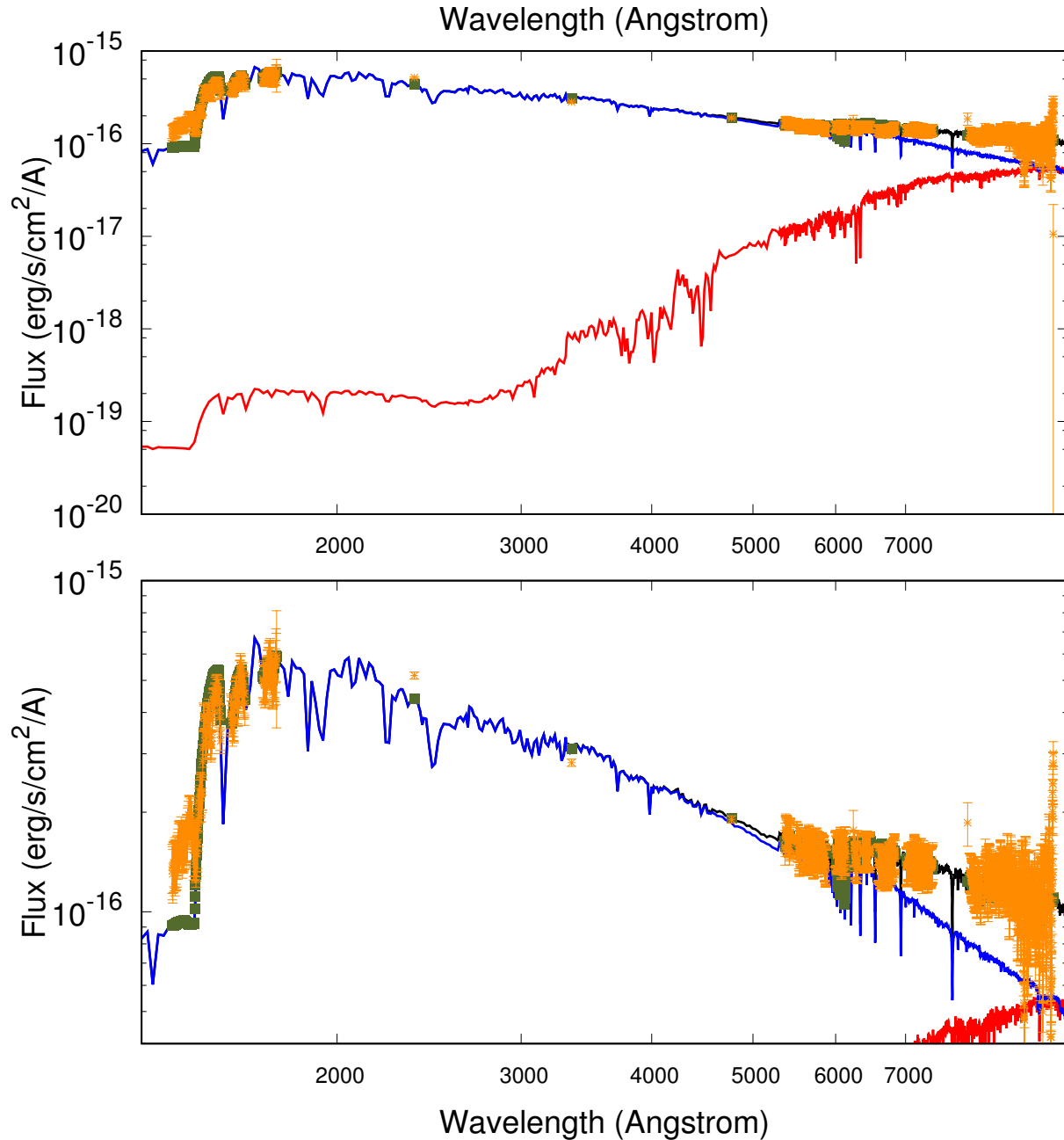


Figure 3. An example best-fit plot of the spectral energy distribution (observed Galactic-extinction corrected flux vs observed-frame wavelength) using the prior $E(B-V) \leq 0.6$, shown by fixing all the discrete parameters and masses to their most-likely values, i.e. the modes of their individual marginal posteriors. Specifically, the model shown here corresponds to SFH=CSF, IMF=Chabrier, $Z_{\text{yup}} = 2.5Z_{\odot}$, $Z_{\text{osp}} = 0.4Z_{\odot}$, extinction law = extragalactic, $E(B-V)=0.6$ and $\tau_{\text{y}} = 45$ Myr. The red and blue curves correspond to the flux contributions from the old and (total) young stellar populations, respectively, and the black curve corresponds to the total spectrum energy distribution (sum of the old and young stellar populations). The green squares correspond to the predicted data and the orange crosses correspond to the observed data. The bottom panel is a zoom-in of the top panel.

Donald et al. (2013) do not point to an internal extinction as high as $E(B-V) = 1.1$. Likewise, as discussed in the next Section, SFR estimates from other independent diagnostics also point to an SFR below $3000 M_{\odot} \text{ yr}^{-1}$. All put together, there is very little observational evidence for models that contribute to such a high SFR, and hence, a cut-off of $SFR < 3000 M_{\odot} \text{ yr}^{-1}$ seems justified.

6.1 Comparison with SFR Estimates from other Diagnostics

Now we compare the SPS-derived SFRs to those derived based on other diagnostics. A concise summary of all the diagnostics can be found in McDonald et al. (2012). Here we mention the two most important diagnostics.

First we consider the $H\alpha$ line emission. Since the $H\alpha$ observations of McDonald et al. (2012) are over a smaller aperture than the $H\beta$ observations of McDonald et al. (2014), we use the $H\beta$ line flux from the latter to calculate the $H\alpha$ line flux. First we assume

the best-fit value $E(B - V) = 0.9$ for the internal extinction and the extra-Galactic extinction law (with $R_V = 4.05$), as preferred by the data with a 100% peak marginalized probability. Using the observed $H\beta$ flux of $7.3 \times 10^{-15} \text{ erg}^{-1} \text{ s}^{-1} \text{ cm}^{-2}$, and assuming the standard case-B (the optical thick limit) recombination ratio of $H\alpha/H\beta = 2.86$, we derive an extinction-corrected $H\alpha$ luminosity of $1.63 \times 10^{44} \text{ erg s}^{-1}$. Using the Kennicutt $H\alpha$ -to-FIR conversion, which assumes a Salpeter IMF and solar metallicity (Kennicutt 1998), we derive a $H\alpha$ -based star formation rate of $1290 M_\odot \text{ yr}^{-1}$. In order to convert this value for a Chabrier or Kroupa IMF, we apply a factor of 1.59 for Chabrier IMF and 1.49 for Kroupa IMF (Madau & Dickinson 2014), and obtain $2048 M_\odot \text{ yr}^{-1}$ and $1925 M_\odot \text{ yr}^{-1}$, respectively. Similarly, if $E(B - V) = 0.6$ instead, as favoured by the Balmer line emission ratios, the corresponding SFRs are $737 M_\odot \text{ yr}^{-1}$ for Salpeter, $1170 M_\odot \text{ yr}^{-1}$ for Chabrier and $1100 M_\odot \text{ yr}^{-1}$ for Kroupa.

Of all the diagnostics, far-infrared (FIR) emission is usually considered the most direct and reliable diagnostic for star formation rate since the FIR photons go through negligible extinction. However, there are two caveats – (a) FIR emission for Phoenix is not very easily measurable due to a significant (dominant) contribution due to the AGN (40%-86% McDonald et al. 2012, 2014; Tozzi et al. 2015) and (b) the conversion relations between FIR luminosity and SFR, such as the Kennicutt FIR-to-SFR relation (Kennicutt 1998), are based on the assumption that all of the ionizing, UV and optical photons are absorbed by the dust and reemitted as far-infrared thermal emission via the photoelectric heating of dust. Under such a scenario, there should be no detectable $\text{Ly-}\alpha$ emission since all $\text{Ly-}\alpha$ photons emitted by the ionized nebular gas surrounding the hot young OB stars should be absorbed by the dust (Mas-Hesse & Kunth 1991). This is not true for Phoenix, which indeed shows a strong $\text{Ly-}\alpha$ line emission.

Keeping the above caveats in mind, we use the total FIR luminosity derived by McDonald et al. (2012), $L_{\text{IR}} = 9.5 \times 10^{12} L_\odot$, which resulted from fitting a single 87 K dust component to *Herschel* PACS and SPIRE data. Assuming a 40% contribution by the AGN (McDonald et al. 2012) results in $L_{\text{IR}} = 3.8 \times 10^{12} L_\odot$ attributed only to stellar heating and assuming a 86% contribution by the AGN (Tozzi et al. 2015) results in $L_{\text{IR}} = 1.3 \times 10^{12} L_\odot$. Now we use the Kennicutt FIR-to-SFR relation, which assumes a Salpeter-type IMF and continuous bursts of age (10-100) Myr, and obtain a star formation rate of $224 M_\odot \text{ yr}^{-1}$ and $654 M_\odot \text{ yr}^{-1}$ for 86% and 40% AGN contributions, respectively. Converting these for Chabrier-type and Kroupa-type IMF implies an SFR of about $(355\text{-}1040) M_\odot \text{ yr}^{-1}$ and $(335\text{-}975) M_\odot \text{ yr}^{-1}$.

The $H\alpha$ emission line yields relatively high SFR estimates but these are subject to internal extinction. The FIR-based SFR estimates, on the other hand, are much lower and not significantly influenced by internal extinction, although these should be considered as a lower limit because of the second caveat mentioned above. Assuming the FIR-estimates to be closer to the true value implies that the internal extinction is likely $E(B - V) \leq 0.6$, which yields the SFR in the range $(454\text{-}494) M_\odot \text{ yr}^{-1}$. Under this scenario, it may very well be that a non-negligible fraction of the Balmer line emission has a non-stellar origin, such as collisional heating and ionization by secondary electrons within the cold filaments produced by the hot ICM via reconnection diffusion (Fabian et al. 2011). If true, this will lower the SFR estimate based on Balmer line emission. The above range of SFR value also agrees well with the SFR of $(530 \pm 53) M_\odot \text{ yr}^{-1}$ that Tozzi et al. (2015) obtained from a detailed analysis of the far-infrared SED.

Lastly, we compare our SFR values to the spectral mass de-

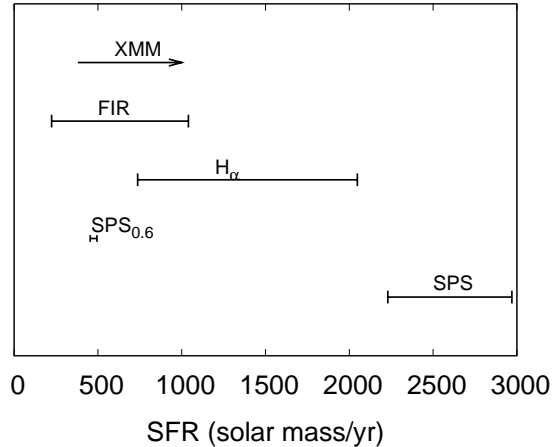


Figure 4. The ranges of SFR values obtained using different diagnostics as discussed in Section 6.1 – (a) stellar population synthesis (SPS) (b) $H\alpha$ and (c) far-infrared emission (FIR). We also show the range of spectral mass deposition rates as obtained with the *XMM-Newton* (XMM). We show the 95% plausible range using SPS for both the cases when no prior on extinction is used and when the prior $E(B-V) \leq 0.6$ (SPS_{0.6}) is imposed.

position rates obtained with the *XMM-Newton* MOS data (Tozzi et al. 2015). According to the best-fit value from the single *MKCFLOW* model in the (0.3-3.0) keV temperature range, the mass deposition rate (MDR) is $[620 (-190 + 200)_{\text{stat}} (-50 + 150)_{\text{syst}}] M_\odot \text{ yr}^{-1}$, once again consistent with the best-fit range of values for $E(B - V) \leq 0.6$. However, Tozzi et al. (2015) found the MDRs to be a function of the temperature, with the MDRs ranging from several $1000 M_\odot \text{ yr}^{-1}$ for (1.8-3.0) keV data to about $380 M_\odot \text{ yr}^{-1}$ for (0.45-0.9) keV data. They concluded that the mass deposition rate found with a single *MKCFLOW* model (assuming single-temperature gas) should not be taken as representative of the entire cooling flow, especially since the gas in Phoenix is observed to cool down to much lower-than ambient temperatures than other cool-core clusters.

The ranges of star formation rate values as derived from different diagnostics are summarized in Figure 4.

6.2 Upper Limit to Star Formation

Now we test whether the best-fit young stellar population adheres to the Eddington limit for star formation (e.g. Scoville et al. 2001), beyond which the stellar radiation pressure on the dust of the stellar burst will exceed the self-gravity of the molecular cloud, causing the dust to disperse. The radiation pressure exceeds self-gravity of the star forming cloud when $(L/M)_{\text{SF}} > 500 L_\odot/M_\odot$, where the subscript “SF” refers to the star forming cloud. McDonald et al. (2014) used the ratio of the FIR luminosity, L_{IR} , to the mass of the molecular hydrogen, M_{H_2} , to calculate the luminosity-to-mass ratio of the star forming cloud as $440 L_\odot/M_\odot$.

One concern with the results where all the parameters are allowed to vary, including the extinction, is the high star formation rate of $2500 M_\odot \text{ yr}^{-1}$ that is obtained. Since we have the synthetic spectra of both the old and the young stellar populations, we can directly estimate an upper limit to the luminosity-to-mass ratio of the star forming cloud given the properties of our best-fit YSP. For this, we calculated the total bolometric luminosity associated with the cumulative YSP (considering all the four bursts a Myr apart) and obtained a value of $L = 4.1 \times 10^{46} \text{ erg s}^{-1} = 1.08 \times 10^{13} L_\odot$. Next

we considered the mass of the molecular hydrogen, M_{H_2} , equal to $(2.2 \pm 8.8) \times 10^{10} M_{\odot}$ as obtained based on the CO(3-2) observations (McDonald et al. 2014). We can now evaluate a lower limit and upper limit of luminosity-to-mass ratio of the star forming site. The lower limit is obtained by considering $L/[M_y + (M_{\text{H}_2})_{\text{UL}}]$, since the mass of the entire star forming cloud is expected to contribute to self-gravity. $(M_{\text{H}_2})_{\text{UL}}$ is the upper limit to M_{H_2} and M_y is the mass of the YSP. The upper limit of $(L/M)_{\text{SF}}$ is obtained by considering $L/(M_{\text{H}_2})_{\text{LL}}$, where we only consider the lower limit to M_{H_2} . Using the above relations, we derive an upper limit of $(L/M)_{\text{SF}}$ as $490 L_{\odot}/M_{\odot}$ and a lower limit of $(L/M)_{\text{SF}}$ as $110 L_{\odot}/M_{\odot}$, both of which conform to the Eddington limit of $500 L_{\odot}/M_{\odot}$. Thus, we do not consider the properties of the YSP, such as the estimated SFR, even when $E(B-V)$ is allowed to be free, to be a problem within the framework of self-regulated star formation. In other words, based on the Eddington limit to star formation, a high value of reddening such as $E(B-V) = 0.9$ that results in a high SFR value can not be ruled out.

6.3 Self-Regulated Heating and Cooling of the ICM

Next we address how the star formation history fits in together with the cooling of the intracluster medium and AGN heating. Not considering any observational priors on the reddening, the SSP models have a higher posterior probability than the CSF models owing to slightly lower χ^2 values. The most probable star formation history model with $E(B-V) = 0.9$ points to a series of four bursts 1 Myr apart. A continuous star formation, on the other hand, that has been onset since 5 Myr ago yields almost similar plausible ranges of values for the model parameters [e.g. the 98% plausible interval for the SFR is $(2220 - 2270) M_{\odot} \text{ yr}^{-1}$]. The SEDs for the two cases are indistinguishable. Therefore we do not make any distinction between the two scenarios. Our code only proves that, mathematically, a model with four bursts that are 1 Myr apart fits the data slightly better than the one with continuous star formation that commenced 5 Myr ago. The Bayes factor (the ratio of the evidence for the two models, SSP and CSF) is about two, which implies that the data do not show any strong preference for one model over the other. On the other hand, imposing an observational prior $E(B-V) \leq 0.6$, the SFH seems to strongly prefer a continuous star formation scenario that has been going on for the last 45 Myr. The SFH reveals a relatively recent star formation activity either way.

In McDonald et al. (2015), the authors claim detection of two pairs of cavities 20 kpc and 100 kpc apart, where the outer “ghost-cavities” have a rather low signal-to-noise, that imply two AGN bursts with a duty cycle of 100 Myr. Irrespective of the two SFH scenarios (SSP/CSF over the last 5 Myr or CSF over the last 45 Myr), assuming that a cooling epoch entails both star formation and blackhole accretion followed by AGN feedback in the form of outbursts that can be traced by X-ray cavities, we do not find any evidence of star formation 100 Myr ago. On the other hand, our code BAYESCOOL currently is not capable of handling complicated star formation histories, such as those containing multiple young stellar populations with a non-periodic separation. For example, our code can not model a composite SED consisting of a 6 Gyr OSP, a 100 Myr YSP and a 5 Myr YSP. Hence, no conclusions may be drawn to confirm the presence of yet another pair of outer cavities. As the next step, we will be making modifications to our code so that such models may be included in the analysis, data permitting.

Assuming the cool-core in Phoenix formed around the same time as other cool cores at around a redshift of 1 (or later) (Hudson et al. 2010), an absence of any star formation between 6 Gyr

and 45 Myr implies a heating mechanism that was very effective at regulating the cold gas in a way that prevented any star formation during that time. Based on a high X-ray photon luminosity, McDonald et al. (2015) posit that the AGN in Phoenix is undergoing a transition from “quasar mode” to “radio-mode”. Our results further corroborate this picture with the quasar-mode as the prime heating mechanism up until recently. As the next step, it would be interesting to see the results from a high-resolution radio image of the AGN at the center of Phoenix so as to investigate the properties of the central AGN, such as its luminosity and age.

6.4 Dust Extinction Law

It is interesting that while the blue-UV slope seems to prefer high extinctions $E(B-V) \sim 1$, the Balmer decrements seem to prefer relatively lower values $E(B-V) \sim 0.6$. The extinction law that best fits the data is the extragalactic law derived from observations of starburst galaxies Calzetti et al. (2000). It is commonly believed that the dust grains in starburst galaxies undergo grain-grain shattering that results in fragmentation of grains into smaller sub-grains (Jones et al. 1996). This process effectively results in a size distribution that is slightly steeper than the standard Mathis, Rumpl, & Nordsieck (MRN) size distribution (Mathis et al. 1977). However, the extragalactic extinction-law is similar to the extinction curve observed for the small magellanic cloud (SMC) in that the starburst activity seems to have modified the dust properties in such a way that has wiped off the small grains responsible for the 2175 Å bump (Gordon et al. 1997, and references therein). At the same time, the small grains resulting in the far-UV extinction rise are not as depleted as in the SMC case. For Phoenix and other cool-core clusters with an abundance of X-rays, there is an additional mechanism, namely, thermal sputtering that disrupts small grains (Draine & Salpeter 1979). Hence, thermal sputtering could potentially act to counter the effects of grain-grain shattering, resulting in an extinction law that is specific to cool-core clusters only. One of our future goals is to investigate whether any of the existing laws actually describes cool-core BCGs well enough. We will do so by allowing the parameters of the extinction law to vary, and including them in the set of discretely-sampled parameters, θ .

7 CONCLUSIONS

Previous studies of Phoenix resulted in the highest measurement of star formation rate for any galaxy, with the estimates reaching up to $1000 M_{\odot} \text{ yr}^{-1}$. However, the number of models considered in those studies is very small ($< 0.01\%$) relative to those considered in this work. Estimating star formation rates is a challenging task, where the main hurdle is exploring the large parameter space. The analysis essentially entails heavy-duty computation with access to multiple computing nodes.

Our Bayesian-motivated SED-fitting code, BAYESCOOL, allows us to probe a large parameter space. Consequently, we are able to explore different star formation histories, i.e. the constituent stellar populations, and their physical parameters. This in turns allows us to put constraints on the values of star formation rates that are plausible. We consider two models for star formation history, instantaneous bursts (SSP) versus continuous star formation (CSF). In addition to that we consider a wide range of ages for the old and the young stellar population with considerable overlap between them. We find that in the absence of any prior except that the $\text{SFR} < 3000 M_{\odot} \text{ yr}^{-1}$ (the predicted cooling-flow rate over the

physical scale of the BCG), the 98% plausible range for the star formation rate lies in the range $2230 - 2890 M_{\odot} \text{ yr}^{-1}$. If we impose a prior on the extinction, $E(B - V) < 0.6$, based on the observational constraints derived by McDonald et al. (2014) using the Balmer line ratios, the best-fit SFR value is much lower and in the range $(454 - 494) M_{\odot} \text{ yr}^{-1}$. We regard this as the most probable range of SFR values for Phoenix.

ACKNOWLEDGMENTS

We thank the anonymous referee for their valuable feedback, time and patience. We thank Prateek Sharma for useful discussions. R. M. sincerely thanks the system administrators, Carsten Aulbert and Henning Fehrmann, at the Albert Einstein Institute for their generous help in setting up the BAYESCOOL code on the computing cluster, ATLAS. R. M. thanks the Albert Einstein Institute for providing academic support for this work. GB acknowledges support for this work from the National Autonomous University of México (UNAM), through grant PAPIIT IG100115. M. M. acknowledges support by NASA through contract HST-GO-13456.002A.

REFERENCES

- Alberts S., Pope A., Brodwin M., Atlee D. W., Lin Y.-T., Dey A., Eisenhardt P. R. M., Gettings D. P., Gonzalez A. H., Jannuzi B. T., Mancone C. L., Moustakas J., Snyder G. F., Stanford S. A., Stern D., Weiner B. J., Zeimann G. R., 2014, *MNRAS*, 437, 437
- Brodwin M., Stanford S. A., Gonzalez A. H., Zeimann G. R., Snyder G. F., et al., 2013, *ApJ*, 779, 138
- Bruzual G., Charlot S., 2003, *MNRAS*, 344, 1000
- Calzetti D., Armus L., Bohlin R. C., Kinney A. L., Koornneef J., Storchi-Bergmann T., 2000, *ApJ*, 533, 682
- Cavagnolo K. W., Donahue M., Voit G. M., Sun M., 2009, *ApJS*, 182, 12
- Conroy C., White M., Gunn J. E., 2010, *ApJ*, 708, 58
- Conselice C. J., et al., 2001, *AJ*, 122, 2281
- Crawford C. S., et al., 1999, *MNRAS*, 306, 857
- Draine B. T., Salpeter E. E., 1979, *ApJ*, 231, 77
- Edge A. C., 2001, *MNRAS*, 328, 762
- Edge A. C., et al., 2002, *MNRAS*, 337, 49
- Edge A. C., Oonk J. B. R., Mittal R., et al., 2010a, *A&A*, 518, L46
- Edge A. C., Oonk J. B. R., Mittal R., et al., 2010b, *A&A*, 518, L47
- Eisenhardt P. R. M., Brodwin M., Gonzalez A. H., Stanford S. A., Stern D., Barmby P., Brown M. J. I., Dawson K., Dey A., Doi M., Galametz A., Jannuzi B. T., Kochanek C. S., Meyers J., Morokuma T., Moustakas L. A., 2008, *ApJ*, 684, 905
- Fabian A. C., Sanders J. S., Williams R. J. R., Lazarian A., Ferland G. J., Johnstone R. M., 2011, *MNRAS*, 417, 172
- Gaspari M., Ruszkowski M., Sharma P., 2012, *ApJ*, 746, 94
- Gordon K. D., Calzetti D., Witt A. N., 1997, *ApJ*, 487, 625
- Heckman T. M., Baum S. A., van Breugel W. J. M., McCarthy P., 1989, *ApJ*, 338, 48
- Hicks A. K., Mushotzky R., 2005, *ApJ*, 635, L9
- Hudson D. S., Mittal R., Reiprich T. H., Nulsen P. E. J., Andernach H., Sarazin C. L., 2010, *A&A*, 513, A37+
- Jarosik N., Bennett C. L., Dunkley J., Gold B., Greason M. R., Halpern M., Hill R. S., Hinshaw G., Kogut A., Komatsu E., et al., 2011, *ApJS*, 192, 14
- Jones A. P., Tielens A. G. G. M., Hollenbach D. J., 1996, *ApJ*, 469, 740
- Kennicutt Jr. R. C., 1998, *ARA&A*, 36, 189
- Larson D., Dunkley J., Hinshaw G., Komatsu E., Nolte M. R., Bennett C. L., Gold B., Halpern M., Hill R. S., et al., 2011, *ApJS*, 192, 16
- Li Y., Bryan G. L., Ruszkowski M., Voit G. M., O'Shea B. W., Donahue M., 2015, *ApJ*, 811, 73
- Madau P., Dickinson M., 2014, *ARA&A*, 52, 415
- Mancone C. L., Gonzalez A. H., Brodwin M., Stanford S. A., Eisenhardt P. R. M., Stern D., Jones C., 2010, *ApJ*, 720, 284
- Mas-Hesse J. M., Kunth D., 1991, *A&AS*, 88, 399
- Mathis J. S., Rumpl W., Nordsieck K. H., 1977, *ApJ*, 217, 425
- Mauch T., Murphy T., Buttery H. J., Curran J., Hunstead R. W., Piestrzynski B., Robertson J. G., Sadler E. M., 2003, *MNRAS*, 342, 1117
- McDonald M., Bayliss M., Benson B. A., Foley R. J., Ruel J., Sullivan P., Veilleux S., Aird K. A., Ashby M. L. N., Bautz M., Bazin G., Bleem L. E., Brodwin M., Carlstrom J. E., Chang C. L., Cho H. M., Clocchiatti A., Crawford T. M., et al., 2012, *Nature*, 488, 349
- McDonald M., Benson B., Veilleux S., Bautz M. W., Reichardt C. L., 2013, *ApJ*, 765, L37
- McDonald M., McNamara B. R., van Weeren R. J., Applegate D. E., Bayliss M., Bautz M. W., Benson B. A., Carlstrom J. E., Bleem L. E., et al., 2015, *ApJ*, 811, 111
- McDonald M., Swinbank M., Edge A. C., Wilner D. J., Veilleux S., Benson B. A., Hogan M. T., Marrone D. P., McNamara B. R., Wei L. H., Bayliss M. B., Bautz M. W., 2014, *ApJ*, 784, 18
- McDonald M., Veilleux S., Rupke D. S. N., 2012, *ApJ*, 746, 153
- McDonald M., Veilleux S., Rupke D. S. N., Mushotzky R., Reynolds C., 2011, *ApJ*, 734, 95
- Mei S., Holden B. P., Blakeslee J. P., Ford H. C., Franx M., Homier N. L., Illingworth G. D., Jee M. J., Overzier R., Postman M., Rosati P., Van der Wel A., Bartlett J. G., 2009, *ApJ*, 690, 42
- Mittal R., et al., 2009, *A&A*, 501, 835
- Mittal R., Hicks A., Reiprich T. H., Jaritz V., 2011, *A&A*, 532, A133
- Mittal R., Oonk J. B. R., Ferland G. J., Edge A. C., O'Dea C. P., Baum S. A., Whelan J. T., Johnstone R. M., Combes F., Salomé P., Fabian A. C., Tremblay G. R., Donahue M., Russell H., 2012, *MNRAS*, 426, 2957
- Mittal R., Whelan J. T., Combes F., 2015, *MNRAS*, 450, 2564
- Moustakas J., Coil A. L., Aird J., Blanton M. R., Cool R. J., Eisenstein D. J., Mendez A. J., Wong K. C., Zhu G., Arnouts S., 2013, *ApJ*, 767, 50
- O'Dea C. P., Baum S. A., Privon G., Noel-Storr J., Quillen A. C., Zufelt N., Park J., Edge A., Russell H., Fabian A. C., Donahue M., Sarazin C. L., McNamara B., Bregman J. N., Egami E., 2008, *ApJ*, 681, 1035
- O'Dea K. P., Quillen A. C., O'Dea C. P., Tremblay G. R., Snios B. T., Baum S. A., Christiansen K., Noel-Storr J., Edge A. C., Donahue M., Voit G. M., 2010, *ApJ*, 719, 1619
- Pfarr J., Maraston C., Tonini C., 2012, *MNRAS*, 422, 3285
- Prasad D., Sharma P., Babul A., 2015, *ApJ*, 811, 108
- Rawle T. D., Edge A. C., Egami E., Rex M., Smith G. P., Altieri B., Fiedler A., Haines C. P., Pereira M. J., Pérez-González P. G., Portouw J., Valtchanov I., Walth G., van der Werf P. P., Zemcov M., 2012, *ApJ*, 747, 29
- Salomé P., Combes F., Revaz Y., Edge A. C., Hatch N. A., Fabian A. C., Johnstone R. M., 2008, *A&A*, 484, 317
- Scoville N. Z., Polletta M., Ewald S., Stolovy S. R., Thompson

- R., Rieke M., 2001, *AJ*, 122, 3017
- Sharma P., McCourt M., Quataert E., Parrish I. J., 2012, *MNRAS*, 420, 3174
- Tozzi P., Gastaldello F., Molendi S., Ettori S., Santos J. S., De Grandi S., Balestra I., Rosati P., Altieri B., Cresci G., Menanteau F., Valtchanov I., 2015, *A&A*, 580, A6
- Tremblay G. R., O’Dea C. P., Baum S. A., Mittal R., McDonald M. A., Combes F., Li Y., McNamara B. R., Bremer M. N., Clarke T. E., Donahue M., Edge A. C., Fabian A. C., Hamer S. L., Hogan M. T., Oonk J. B. R., Quillen A. C., Sanders J. S., Salomé P., Voit G. M., 2015, *MNRAS*, 451, 3768
- Ueda S., Hayashida K., Anabuki N., Nakajima H., Koyama K., Tsunemi H., 2013, *ApJ*, 778, 33
- van Dokkum P. G., 2001, *PASP*, 113, 1420
- Walcher J., Groves B., Budavári T., Dale D., 2011, *Ap&SS*, 331, 1
- Williamson R., Benson B. A., High F. W., Vanderlinde K., Ade P. A. R., Aird K. A., Andersson K., Armstrong R., Ashby M. L. N., Bautz M., Bazin G., Bertin E., Bleem L. E., Bonamente M., Brodwin M., Carlstrom J. E., et al., 2011, *ApJ*, 738, 139